

Solution of an Acoustic Transmission Inverse Problem by Extended Inversion

William W. Symes¹, Huiyi Chen² and Susan E. Minkoff²

¹ *PO Box 43, Orcas, WA 98280 USA*

² *Department of Mathematical Sciences, FO 35, University of Texas at Dallas, Richardson, TX 75080 USA*

25 January 2022

ABSTRACT

Study of a simple single-trace transmission example shows how an extended source formulation of full-waveform inversion can produce an optimization problem without spurious local minima (“cycle skipping”), hence efficiently solvable via Newton-like local optimization methods. The data consist of a single trace extracted from a causal pressure field, propagating in a homogeneous fluid according to linear acoustics, and recorded at a given distance from a transient point energy source. The source intensity (“wavelet”) is presumed quasi-impulsive, with zero energy for time lags greater than a specified maximum lag. The inverse problem is: from the recorded trace, recover both the sound velocity or slowness and source wavelet with specified support, so that the data is fit with prescribed RMS relative error. The least-squares objective function has multiple large residual minimizers. The extended inverse problem permits source energy to spread in time, and replaces the maximum lag constraint by a weighted quadratic penalty. A companion paper shows that for proper choice of weight operator, any stationary point of the extended objective produces a good approximation of the global minimizer of the least squares objective, with slowness error bounded by a multiple of the maximum lag and the assumed noise level. This paper summarizes the theory developed in the companion paper and presents numerical experiments demonstrating the accuracy of the predictions in

concrete instances. We also show how to dynamically adjust the penalty scale during iterative optimization to improve the accuracy of the slowness estimate.

Key words: full waveform inversion, extended source inversion, cycle skipping

1 INTRODUCTION

Model-based parameter estimation by least squares data fitting is a widely used and successful technique for data analysis in science and engineering (Bertero & Boccacci, 1998; Vogel, 2002), and particularly in the geosciences (Parker, 1994; Tarantola, 2005). In its application to seismology, least-squares data fitting has come to be known as Full Waveform Inversion (FWI) and is now well-established as a useful tool for probing the Earth’s subsurface (Virieux & Operto, 2009; Fichtner, 2010; Schuster, 2017). However, FWI encounters a serious practical obstacle, so-called “cycle-skipping”. This term signifies the tendency of the mean-square error function to exhibit approximate stationary points far from a global optimum. Because of the typical dimensions of field FWI problems, only local gradient-based minimization algorithms are computationally practical. These methods find approximate stationary points (or local minima), so may stagnate at suboptimal and geologically uninformative Earth models. Local descent methods avoid suboptimal stagnation only if initial models are already quite close to optimal, in the sense of predicting the arrival times of seismic events to within a small multiple of the dominant data wavelength (Gauthier et al., 1986; Virieux & Operto, 2009; Plessix et al., 2010).

This paper examines one of a number of proposed alternatives to least squares FWI, based on an extension of the model-to-data mapping (“extended inversion”), in the context of a very simple acoustic transmission inverse problem: the sound velocity in a homogeneous fluid is to be determined from a single recording of a pressure wave emitted at a known location around a known time, and propagated over a known distance. In a companion paper (Symes, 2022), we show precisely how descent-based FWI fails to solve this problem absent a very good initial model estimate and precisely why extended inversion succeeds, using the same type of optimization, and from an essentially arbitrary initial model estimate. The companion paper gives detailed estimates for the accuracy of the sound velocity determination in terms of the time extent of the energy

excitation and the signal-to-noise ratio of the data. In this paper we describe these theoretical results succinctly and illustrate the mathematical conclusions with relevant numerical examples.

Model extension is an old idea in seismic data processing (Symes, 2008). In recent years, many extended inversion algorithms have been proposed as cures for cycle-skipping (Symes & Carazzone, 1991; Plessix et al., 2000; Symes, 2009; Luo & Sava, 2011; Biondi & Almomin, 2012; van Leeuwen & Herrmann, 2013; Liu et al., 2014; Warner & Guasch, 2014; Lameloise et al., 2015; Warner & Guasch, 2016; van Leeuwen & Herrmann, 2016; Chauris & Cocher, 2017; Symes & Hou, 2018; Aghmiry et al., 2020; Métivier & Brossier, 2020). The approach studied in this paper uses *source extension*: the energy source component of the experimental model is permitted to have more (or less constrained) parameters than the experimental design suggests. Huang et al. (2019) give an overview and taxonomy of source extension methods.

This work differs in a crucial respect from the works cited above. In all of those papers the authors use numerical tests with synthetic and/or field data to justify their conclusions about how the methods avoid cycle-skipping. Of course, numerical examples provide retrospective evidence, which in itself cannot guarantee that another test will not produce a substantially different result. In fact, Symes (2020) showed that one of these approaches, believed for several years to be immune to cycle-skipping, is in some cases no better in that respect than FWI.

The theoretical results presented in the companion paper (Symes, 2022) provide the missing guarantee. These results, reviewed in the next section, explain circumstances under which the extended inversion algorithm developed below will succeed in producing an accurate model estimate starting with an arbitrary initial guess. Our numerical examples illustrate essential features of this theory. Some of the error bounds are sharp, and we give examples that underline such conclusions. In other cases the theory gives sufficient conditions which may not be necessary under practically interesting limitations on the data beyond the basic assumptions of the theory. We illustrate such opportunities for further theoretical development as well.

Extended inversion is not the only alternative to straightforward least-squares data fitting that may overcome cycle-skipping. For example, evidence has recently emerged that the Wasserstein metric arising in the theory of optimal transport may provide a measure of error between model-

predicted and observed seismic data that is less oscillatory than the mean-square error (Yang et al., 2018; Métivier et al., 2018). Very recently, Mahankali & Yang (2021) have developed theoretical results analogous to ours, showing convexity of the Wasserstein-2 error function in several simple examples.

In the next (“Theory”) section, we describe the conceptual framework of this inverse problem, review the related literature, and state the essence of our main theoretical results as established in Symes (2022). The theory is illustrated in the “Numerical Experiments” Section that follows.

2 THEORY

In this section we describe the theoretical results which we will illustrate with numerical experiments in the next section.

2.1 Background and Problem Description

The physical setting of our study is constant-density acoustic wave propagation in a 3D homogeneous medium in which the (single) mechanical parameter of interest used to describe the Earth is the speed of sound, or for our purposes the reciprocal wave velocity or slowness, $m > 0$.

The source of acoustic energy is localized at a point in space and radiates uniformly in all directions with time-dependent intensity (“wavelet”) $w(t)$, thereby generating a pressure field, $p(\mathbf{x}, t)$. Both the pressure field and the wavelet vanish at large negative times. The data consists of a recording of the pressure field at a single receiver located a distance, r , from the source, over the time interval $[t_{\min}, t_{\max}]$. The pressure field solves the wave equation (Friedlander, 1958):

$$\begin{aligned} \left(m^2 \frac{\partial^2}{\partial t^2} - \nabla^2 \right) p(\mathbf{x}, t) &= w(t) \delta(\mathbf{x} - \mathbf{x}_s) \\ p(\mathbf{x}, t) &= 0, \quad t \ll 0. \end{aligned} \tag{1}$$

The solution p of the problem 1 is given by the well-known expression (Courant & Hilbert (1962), Chapter VI, section 12, equation 47):

$$p(\mathbf{x}, t) = \frac{1}{4\pi|\mathbf{x} - \mathbf{x}_s|} w(t - m|\mathbf{x} - \mathbf{x}_s|). \tag{2}$$

The predicted pressure at the receiver point, \mathbf{x}_r , is

$$p(\mathbf{x}_r, t) = \frac{1}{4\pi r} w(t - mr) = F[m]w(t). \quad (3)$$

The mapping $F[m]$ so defined (ignoring the amplitude factor $1/(4\pi r)$) is an m -dependent time shift, which is the basis of many illustrations of the cycle-skipping phenomenon (for example, see Virieux & Operto (2009), Figure 7). It is unsurprising, therefore, that an analysis of cycle-skipping can be rooted in the simplified setting we describe. A naive version of the inverse problem investigated in this paper would be: given recorded data d , find m and w so that $F[m]w \approx d$.

Clearly this problem statement is not interesting as it stands, since fitting the data does not constrain the slowness m at all: for any m , the choice $w(t) = 4\pi r d(t + mr)$ yields $F[m]w = d$ exactly. To be useful, the problem statement must be augmented with a constraint on the model (m, w) . One natural constraint is to assume that w is non-zero only for small times: a maximum time lag (“support radius”) $\lambda > 0$ exists so that $w(t) = 0$ for $|t| > \lambda$.

An assumption that w is non-zero only for small $|t|$ may be justified as follows. Seismic sources may act over considerable time intervals. An example from exploration seismology is the airgun, which produces an oscillating pressure pulse that dies away slowly. It is commonplace to estimate this pulse, usually by recording the emitted pressure field at a position where it should nominally be isolated from other signal, then deconvolve it from the data by safeguarded Fourier division or other means, with appropriate compensation for the relative positions of the pulse recording and the zone of interest within the earth. This so-called signature deconvolution (Ziolkowski et al. (1982); Sheriff & Geldart (1995), section 9.5 and Yilmaz (2001), Chapter 2) results in modified data corresponding to a source equal to signature deconvolution of the pulse estimate itself. The deconvolved source pulse approximates an impulse ($\delta(t)$). It cannot actually be an impulse, due to the finite frequency nature of seismic data, but its amplitudes are typically small outside of a much smaller time interval than is the case for the original pulse estimate.

This reasoning leads us to incorporate specification of a maximum time lag or support radius λ into the statement of the inverse problem. To state the problem precisely, we use the standard

notation $\|u\|^2$ for the square integral (“ L^2 norm squared”) of any function u of time:

$$\|u\|^2 = \int_{-\infty}^{\infty} dt u(t)^2. \quad (4)$$

Inverse Problem: *given data d , assumed data noise level $\epsilon \in [0, 1)$, extremal slownesses $0 < m_{\min} \leq m_{\max}$ and support radius $\lambda > 0$, find $m \in [m_{\min}, m_{\max}]$ and w vanishing for $|t| > \lambda$, so that*

$$\|F[m]w - d\| \leq \epsilon \|d\|. \quad (5)$$

2.2 Full Waveform Inversion

Despite its simplicity, this problem exhibits the pathology characteristic of field-scale FWI when formulated as a least-squares optimization problem.

Given a data trace d and maximum lag $\lambda > 0$, we introduce three versions of the least squares (FWI) objective function for the single-trace transmission problem:

Definition 1. *The basic FWI objective function e of slowness m and wavelet w is*

$$e[m, w; d] = \frac{1}{2} \frac{\|F[m]w - d\|^2}{\|d\|^2} \quad (6)$$

Definition 2. *The reduced FWI objective \tilde{e} of slowness m is*

$$\tilde{e}[m; d] = \min_w e[m, w; d], \quad (7)$$

the minimum being taken over all w with $w(t) = 0$ for $|t| > \lambda$.

Definition 3. *Given a wavelet w_* with $w_*(t) = 0$ for $|t| > \lambda$, the restricted FWI objective with $w = w_*$ is the function of m given by $e[m, w_*; d]$.*

Result 1. *Suppose that $m_* > 0$, $\lambda > 0$, $w_*(t) = 0$ for $|t| > \lambda$, and $d = F[m_*]w_*$. If $m \neq m_*$, then $\tilde{e}[m; d]$ and $e[m, w_*; d]$ are both > 0 . If $|m - m_*| \geq 2\lambda/r$, then*

$$\tilde{e}[m; d] = e[m, 0; d] = 1/2$$

and

$$e[m, w_*; d] = 1.$$

That is, both the reduced FWI objective \tilde{e} (minimizer of e over w for each m) and the restricted FWI objective $e[\cdot, w_*; d]$ (using the same wavelet w_* as used to generate the noise-free data) have entire intervals of local minimizers for m sufficiently far from the slowness m_* used to generate the data, which is also the global minimizer of both. Under the conditions we have posed, the minimum in equation (7) is attained. Therefore any local minimizer of \tilde{e} corresponds to at least one local minimizer of e . Consequently e also has a continuum of local minimizers. These local optima are far from the global minimizer m_* (or global minimizer (m_*, w_*) in the case of e) and have 50% and 100% error levels respectively, for noise-free data. Local optimization of any of these objectives therefore fails to solve the Inverse Problem stated above for any $\epsilon < 1/2$, unless the initial estimate of m is within $2\lambda/r$ of the global minimizer m_* . This phenomenon is what is meant by “cycle-skipping”.

The observation, that (locally) minimizing \tilde{e} over m corresponds to minimizing e over (m, w) , suggests a *nested* approach: inner minimization over w (to compute \tilde{e}) and outer minimization (of \tilde{e}) over m . This nested algorithm is an example of the *Variable Projection Method* (or “VPM”), in the nomenclature introduced by Golub & Pereyra (1973, 2003). Several authors have observed that VPM may be more computationally efficient for FWI problems (including source estimation) than direct application of local optimization algorithms to e . In fact, the sensitivity of e to perturbations in source parameters (like w) tends to be very different from its sensitivity to perturbations in kinematic medium parameters (such as m). The nested iteration segregates these sensitivities and reduces ill-conditioning and resulting computational inefficiency (Aravkin & van Leeuwen, 2012; Li et al., 2013; Huang, 2016). VPM is the main computational device used in our examples. It also plays a central role in the theory developed in the companion paper.

2.3 Extended Source Inversion

“Extension”, as used in this paper, means provision of additional degrees of freedom in the domain of the modeling operator (such as F) with the intent of generating more paths avoiding local minima and leading to a solution of the Inverse Problem. The extension discussed here consists in dropping the support constraint on w , thus considerably enlarging the space of feasible models. In fact, as noted above, the extended model space is then so large that perfect data fit is possible with any m . To compensate for the resulting indeterminacy in the estimation of m , we add a quadratic penalty term to the least squares objective, e , defined by a penalty operator A and penalty weight α .

Definition 4. *The Extended Source Inversion (“ESI”) objective function J_α is defined by*

$$g[w] = \frac{1}{2} \|Aw\|^2 / \|d\|^2, \quad (8)$$

$$\begin{aligned} J_\alpha[m, w; d] &= e[m, w; d] + \alpha^2 g[w] \\ &= \frac{1}{2} (\|F[m]w - d\|^2 + \alpha^2 \|Aw\|^2) / \|d\|^2. \end{aligned} \quad (9)$$

The normalizations by the data norm $\|d\|$ in the equations (6), (8), and (9) make the values of e , $\alpha^2 g$, and J_α nondimensional and simplify the interpretation of numerical examples.

The penalty operator A must penalize nonzero values of w for large $|t|$ since we search for a wavelet that is only active in a short time interval centered at $t = 0$. One simple choice for A is

$$(Aw)(t) = tw(t). \quad (10)$$

We will assume A is of this form throughout the paper. The penalty weight α also must be chosen, and we will discuss the choice of α in the next subsection.

While minimization of the ESI objective J_α might be tackled directly - by alternating minimizations over m and w or by computing updates for m and w simultaneously - we have already noted that e , a component of J_α , has dramatically different sensitivity to m versus w , and therefore so does J_α . Therefore we employ the Variable Projection Method described above, with an inner minimization of J_α over w , followed by an outer minimization over m . Any minimizer w of

$J_\alpha[m, \cdot; d]$ must solve the *normal equation*

$$(F[m]^T F[m] + \alpha^2 A^T A)w = F[m]^T d. \quad (11)$$

With the definitions of F and A given above, the normal equation has a unique solution. Therefore $J_\alpha[m, \cdot; d]$ has a unique minimizer $w = w_\alpha[m; d]$.

Definition 5. The reduced ESI objective \tilde{J}_α is

$$\tilde{J}_\alpha[m; d] = \inf_w J_\alpha[m, w; d] = J_\alpha[m, w_\alpha[m; d]; d]. \quad (12)$$

Result 2. Let $d_* = F[m_*]w_*$ be noise-free data with target slowness $m_* > 0$ and target wavelet $w_*(t) = 0$ for $|t| > \lambda$. Let $d = d_* + n$ be noisy data, with noise trace n . Define the noise-to-signal ratio η by $\eta = \|n\|/\|d_*\|$. If $\alpha > 0$ and $\eta < \frac{\sqrt{5}-1}{2}$, then any stationary point m of $\tilde{J}_\alpha[\cdot; d]$ satisfies

$$|m - m_*| \leq (1 + f(\eta)) \frac{\lambda}{r}, \quad (13)$$

where $f(\eta) = \frac{2\eta(1+\eta)}{1-\eta(1+\eta)} = 2\eta + O(\eta^2)$.

In particular, if the data is noise-free, that is $\eta = 0$, then the error between any stationary point of the reduced ESI objective \tilde{J}_α and the target slowness m_* is at most the maximum lag λ of the target wavelet w_* divided by the source-receiver offset r . Note the dramatic contrast with the least-squares estimation (minimization of e as in 6). As indicated in Result 1, the reduced FWI objective has stationary points at arbitrarily large differences from the target slowness.

No general bounds can hold for much larger noise levels than indicated in Result 2. For instance, $n = -F[m_*]w_*$ ($\eta = 1$) yields $d = 0$, for which any m is a stationary point. However, numerical exploration suggests that stronger bounds might hold given other constraints on data error. A natural example is uniformly distributed random noise filtered to have the same spectrum as the source. Numerical Experiment 5 below illustrates this case, for which the only stationary point of the reduced ESI objective is a quite precise estimator of the target slowness.

Unless the data is noise-free, the estimated wavelet $w_\alpha[m; d]$ (solution of the normal equation

(11)) corresponding to a stationary point m of $\tilde{J}_\alpha[\cdot; d]$ need not vanish for $|t| > \lambda$. To construct a solution of the Inverse Problem, we must modify the wavelet $w_\alpha[m, d]$.

Result 3. *Define*

$$\mathbf{1}_{[-\lambda, \lambda]}(t) = \begin{cases} 1, & |t| \leq \lambda \\ 0, & \text{else.} \end{cases}$$

Suppose that $\mu > 0$, $d = F[m_]w_* + n$ with $w_*(t) = 0$ for $|t| > \mu$, and m is a stationary point of $\tilde{J}_\alpha[\cdot; d]$. Then the pair $(m, \mathbf{1}_{[-\lambda, \lambda]}w_\alpha[m, d])$ solves the Inverse Problem (5), that is*

$$e[m, \mathbf{1}_{[-\lambda, \lambda]}w; d] \leq \frac{1}{2}\epsilon^2,$$

provided that

$$\lambda \geq (2 + f(\eta))\mu, \tag{14}$$

$$\epsilon \geq \frac{(8\pi r \alpha \mu)^2}{1 + (8\pi r \alpha \mu)^2} + \eta. \tag{15}$$

Thus the minimization of the extended objective J_α provides a solution of the Inverse Problem with constraints on the achievable performance and bounds on the errors.

2.4 The discrepancy algorithm

So far in this story, the selection of the penalty weight α has played a relatively minor role. On the other hand, in practical calculations selection of α strongly influences the convergence of iterative methods and the quality of the results. Concentration of the wavelet near $t = 0$ clearly favors larger α . In fact the reduced penalty term $g[m, w_\alpha[m; d]; d]$ is a decreasing function of α for any m . As g measures the dispersion of the wavelet away from $t = 0$, larger α is to be preferred, all else being equal. However all else is not equal: the data error $e[m, w_\alpha[m; d]; d]$ is an increasing function of α , so α is constrained by data fit. The choice of α affects the reduced ESI objective $\tilde{J}_\alpha[m; d]$ and, therefore, the estimation of the nonlinear variable m as well:

Result 4. *Assume once again that $d_* = F[m_*]w_*$, $d = d_* + n$ with $w_*(t) = 0$ for $|t| > \lambda$ and*

noise-to-signal ratio $\eta = \|n\|/\|d_*\|$, and suppose that m is a stationary point of $\tilde{J}_\alpha[\cdot; d]$. Then

$$|m - m_*| \leq \frac{\lambda}{r} + \frac{\eta}{\alpha}(\dots), \quad (16)$$

in which the elided quantity is polynomial in α with positive constant term.

That is, stationary points of \tilde{J}_α become more accurate approximations of the target slowness m_* as α increases, at least for small α .

These observations motivate an algorithm for selection of α , based on a version of the *discrepancy principle* (Engl et al., 1996; Hanke, 2017; Fu & Symes, 2017), adapted to the setting of this paper, namely m and α should solve the

Discrepancy Problem: given data $d \in D$ and a range of minimum and maximum allowable errors $0 < e_- < e_+$, find the slowness m and the scalar α so that

- (i) m is a stationary point of the reduced objective function $\tilde{J}_\alpha[\cdot; d]$, and
- (ii) $e_- < e[m, w_\alpha[m; d]; d] < e_+$.

(“Discrepancy” is used here as a synonym for “data misfit”, as measured by e .)

We use an alternating, or coordinate search, *discrepancy algorithm* for solution of this problem, combining a local optimization algorithm for updating m , and an algorithm for updating α . A first version of the discrepancy algorithm appeared in Fu & Symes (2017).

Note that the mean square error, e , lies in the interval (e_-, e_+) at a solution of this problem. Use of an interval, rather than a single target error level, accomplishes two objectives:

- it is consistent with the general lack of precise knowledge of data error in most applications;
- it permits a local optimization algorithm to make several small updates of m before an update of α is required.

In general, lack of an obvious rule for selection of an initial α obstructs the use of the discrepancy principle for penalty formulations of many inverse problems. A common solution is a more or less arbitrary initial selection followed by repeated objective evaluation at a geometric sequence, or a

bisection series, of weights until one is found for which the required quantity lies in the specified interval.

The extended inverse problem studied here has a remarkable property that eliminates this obstruction: a useful initial α value for the problem studied here is simply $\alpha = 0$. Since the modeling operator $F[m]$ is surjective for any $m > 0$, as noted earlier, this choice yields $e[m, w_0[m; d]; d] = 0$ for any initial m (which may therefore be chosen arbitrarily). Thus the upper bound on e in condition (ii) of the Discrepancy Problem is trivially satisfied.

To get the data misfit into the prescribed range (satisfy the lower bound in condition (ii)) and to update it after subsequent updates of m , we use the

Basic Alpha Update Rule: *given an initial value α_0 of α , generate a sequence $\{\alpha_k : k = 0, 1, 2, \dots\}$ by the recursion*

$$\alpha_{k+1} = \left(\alpha_k^2 + \frac{e_+ - e[m, w_{\alpha_k}[m; d]; d]}{2g[w_{\alpha_k}[m; d]]} \right)^{1/2}, \quad (17)$$

first suggested by Fu & Symes (2017).

Symes (2021) shows (Appendix A) that e is increasing in α and that the sequence of α produced by the update rule 17 generates an increasing sequence of e in the interval $[0, e_+]$ with e_+ as its only accumulation point, hence attaining the target interval $[e_-, e_+]$ in a finite (and estimable) number of steps. Convergence can be accelerated by a number of devices. However in the examples reported in the next section, we have used the basic rule 17.

Having updated α , the algorithm updates m by one or more steps of a local optimization algorithm. In the examples presented below, we have used Brent's method (Brent, 1971) to search for a zero of the gradient.

After the α update cycle, the error bounds are satisfied, that is, $e[m, w_\alpha[m; d]; d] \in (e_-, e_+)$, but the m update is likely to reduce e , as it is a summand in the definition of \tilde{J}_α . If e is reduced below e_- then control passes to the α update. If an approximate local minimizer is detected, then the algorithm terminates if the error bounds are satisfied, or passes to the α update if not. Thus α is steadily increased, resulting in increasing accuracy of the m estimate, while the data misfit is kept

within the prescribed range. The next section recounts several uses of this discrepancy algorithm, illustrating its behaviour in detail.

2.5 Solving the Inverse Problem

Our goal is to solve the Inverse Problem stated at inequality (5). That is, to determine a source w with prescribed support $\subset [-\lambda, \lambda]$ and the slowness m in a prescribed interval $[m_{min}, m_{max}]$, so that the RMS data error $\|F[m]w - d\|$ is less than a prescribed multiple of $\|d\|$. Merely finding a stationary point of the reduced ESI objective function \tilde{J}_α does not accomplish this goal, even though it yields a good slowness estimate under many circumstances, both because the wavelet $w_\alpha[m; d]$ so obtained does not in general vanish for $|t| > \lambda$, and because the stationarity condition does not constrain data error.

We propose an algorithm for solving the Inverse Problem via ESI that addresses both of these shortcomings, consisting of two steps. In the first step we use the discrepancy algorithm, described in the previous subsection, to adjust the penalty weight α dynamically, in the course of minimization of the reduced ESI objective \tilde{J}_α (thus estimating the wavelet $w = w_\alpha[m; d]$ at the same time). The discrepancy algorithm maintains an upper bound on data error e throughout the minimization of \tilde{J}_α , and simultaneously maximizes α , thus minimizing wavelet energy dispersion away from $t = 0$. The second step of the algorithm, truncation of the wavelet to the prescribed maximum lag $|t| \leq \lambda$ as in Result 3, therefore modifies the wavelet as little as possible, and in turn increases the data error as little as possible.

The reasoning just stated is partly heuristic; the theory developed in the companion paper (Symes, 2022) does not directly address the performance of this algorithm. Result 3 states sufficient conditions on the data error and maximum lag under which a stationary point of J_α will solve the Inverse Problem but does not really explain the role of α or of the discrepancy algorithm for controlling it. Instead, in this paper we include a pair of examples, at the end of the next section, which suggest that our approach has some promise.

3 NUMERICAL EXAMPLES

This section presents numerical examples that illustrate the theoretical results described in the previous section. The examples are divided into two sets. The first set (Experiments 1-5) explores the location of stationary points for both FWI and ESI. The results of these experiments conform to the predictions of the theoretical Results 1 and 2. The second set (Experiments 6 and 7) present an implementation of the discrepancy algorithm and show how it can be used in conjunction with ESI to solve the Inverse Problem using the algorithm sketched at the end of the previous section. These last two examples illustrate Results 3 and 4.

In each numerical experiment, as in the theory, waves are generated by a single source, and data is recorded at a single receiver. The source and receiver are located 1 km apart ($r = |x_r - x_s| = 1$ km). Unless noted otherwise, the target wavelet $w_*(t)$ is a the truncation of a zero phase Ricker wavelet with peak frequency 40 Hz, truncated to have support radius $\mu = 0.025$ s (see Figure 1). The target slowness is $m_* = 0.4$ s/km. We choose a noise trace n , and add it to the noise-free data predicted by m_* and w_* , to obtain data traces $d = F[m_*]w_*(t) + n(t) = \frac{1}{4\pi r}w_*(t - m_*r) + n(t)$, recorded over the interval $[0.25, 0.65]$ s.

Explicit expressions for the reduced objective function \tilde{J}_α and its gradient $\frac{d}{dm}\tilde{J}_\alpha$ are:

$$\tilde{J}_\alpha[m; d] = \frac{1}{2\|d\|^2} \int_{t_{\min}}^{t_{\max}} dt (4\pi r \alpha(t - mr))^2 (1 + (4\pi r \alpha(t - mr))^2)^{-1} d(t)^2, \quad (18)$$

$$\frac{d}{dm}\tilde{J}_\alpha[m; d] = -\frac{(4\pi r \alpha)^2}{\|d\|^2} \int_{t_{\min}}^{t_{\max}} dt (t - mr) (1 + (4\pi r \alpha(t - mr))^2)^{-2} d(t)^2. \quad (19)$$

These two expressions are based on Definition 5 and the Green's function in equation (3). A detailed derivation can be found in (Symes, 2022). Here we approximate these integrals by the trapezoidal rule with $[t_{\min}, t_{\max}] = [0.25, 0.65]$ s. Since the frequency of the Ricker wavelet is 40 Hz, its wavelength is 0.025 s. We pick a step size of $dt = 0.001$ resulting in 25 grid points per wavelength.

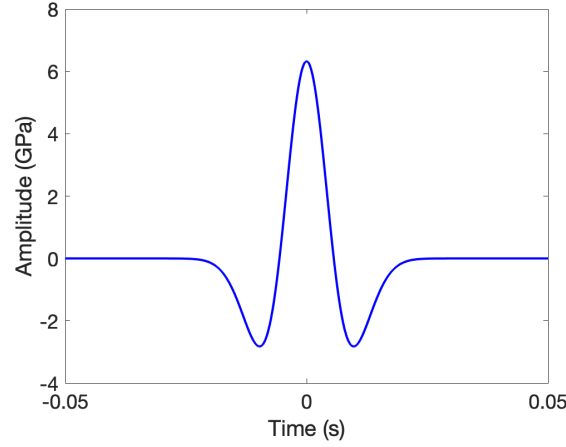


Figure 1. 40 Hz Ricker wavelet centered at $t = 0$.

3.1 Stationary Points

In the five experiments discussed in this subsection, we explore the locations of stationary points for restricted and reduced FWI and reduced ESI objective functions and their dependence on data noise-to-signal level η and properties of the target wavelet w_* . In all cases the penalty weight $\alpha = 1$.

Experiment 1: Noise Free Data

In this experiment the data is noise-free (noise-to-signal ratio η is equal to 0). Figure 2 displays the data $d = F[m_*]w_*(t)$. Figure 3 shows the restricted FWI objective function (Definition 3) using the target wavelet w_* , in blue and the reduced ESI objective function (Definition 5) in red, as functions of slowness. We see that the restricted FWI objective function has infinitely many local minima, in the regions $[0.25, 0.35]$ and $[0.45, 0.63]$ s/km, consistent with Result 1 with $\lambda = 0.025$ s, along with several other stationary points nearer the target slowness. This plot is similar to many examples in the literature illustrating the tendency of FWI to cycle-skip, thus rendering local optimization ineffective. In contrast, the reduced ESI objective function exhibits only one local minimum, at the target slowness, consistent with Result 2.

Experiments 2a & 2b: Noise Free Data, Shifted Wavelet These examples show that the bounds mentioned in Result 2 are sharp and that the reduced (rather than restricted) FWI objective defined in Definition 2 behaves as indicated in Result 1.

The target wavelet for experiment 2a is the wavelet of experiment 1 (Figure 1), shifted by 0.01

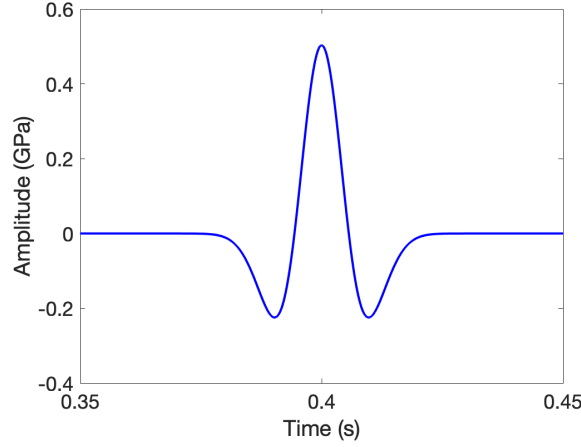


Figure 2. Experiment 1: data.

s, see Figure 4. The target wavelet for experiment 2b is shifted further, by 0.05 s. Both wavelets are supported in the interval $[-0.1, 0.1]$ s, so we use $\lambda = 0.1$ s here. The target slowness is still $m_* = 0.4$ s/km. The noise-free data for experiment 2a is shown in shown in Figure 5. The red curves in Figures 6 and 7 show that in both cases, the estimated slowness m is in error by less than 0.1 s/km, consistent with Result 2. The error in the second case (0.05 s/km) is larger than the error in the first case (0.01 s/km, see Figure 8). By changing the wavelet shape and piling up its energy near the support limit $\lambda = 0.1$, we could obtain an error arbitrarily close to the bound 13. That is, the bound in Result 2 is sharp.

The blue curves in Figures 6 and 7 show the reduced FWI objective \tilde{e} . Definition 2 shows that the assumed maximum lag λ plays a central role in the computation of \tilde{e} . The minimum is taken

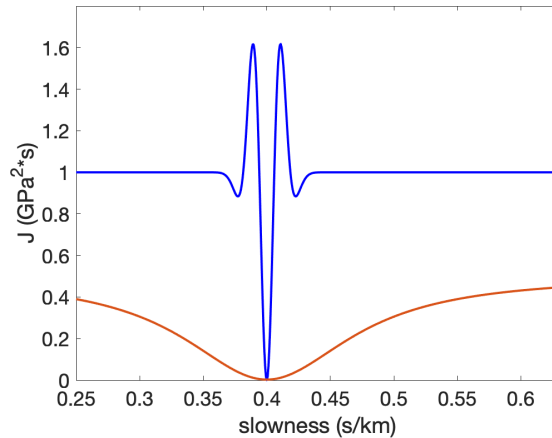


Figure 3. Experiment 1: the restricted FWI (blue curve) and reduced ESI (red curve) objective functions versus slowness.

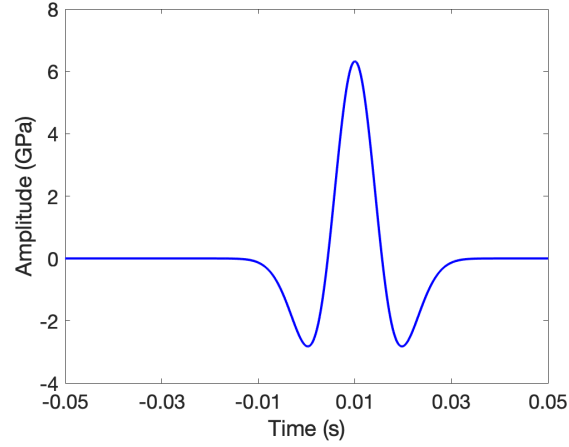


Figure 4. Target wavelet for Experiment 2a with peak amplitude at $t = 0.01$ s.

over all wavelets with support in $[-\lambda, \lambda]$. Result 1 predicts that $\tilde{e} = 1/2$ for $|m - m_*| > 2\lambda/r = 0.2$ s/km for the choices made in these examples, and reference to the figures shows that this prediction holds.

Minimization of the reduced ESI objective for the data of experiment 2a converged quickly to $m \approx 0.41$ from an initial estimate of $m = 1/3$, and produced the wavelets shown in Figure 9. The predicted data also converged quickly to a final iterate closely matching the target data, as shown in Figures 10 and 11.

Experiment 3: 30% Coherent Noise Figure 12 displays the result of adding coherent noise to the data used in Experiment 1. This coherent noise is a small-amplitude shifted 40 Hz Ricker wavelet

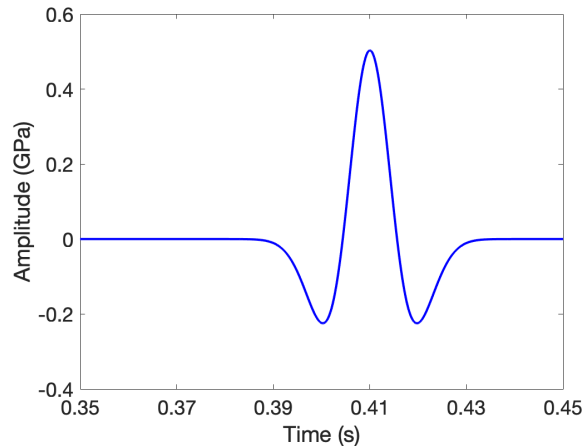


Figure 5. Noise-free data used in Experiment 2a.

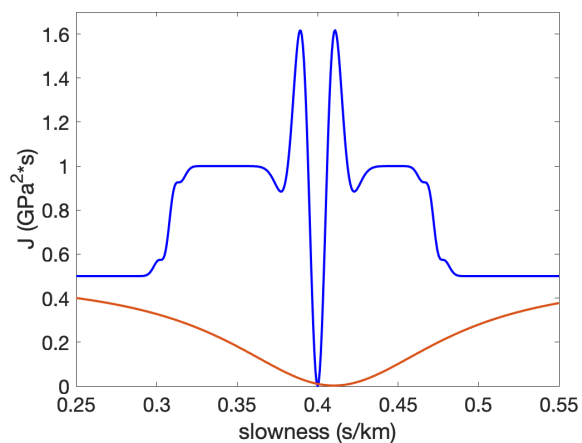


Figure 6. Experiment 2a: reduced FWI (blue curve) and reduced ESI (red curve) objective functions versus slowness.

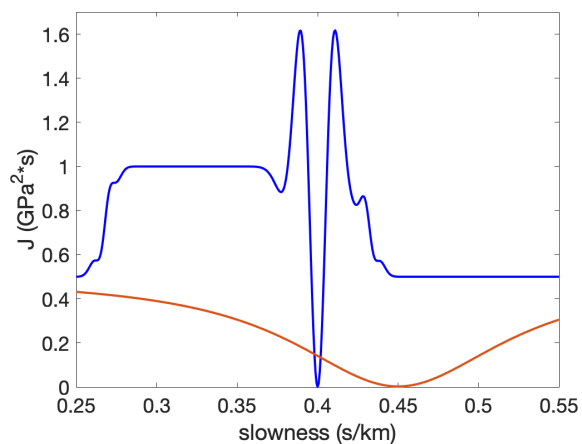


Figure 7. Experiment 2b: reduced FWI (blue curve) and reduced ESI (red curve) objective functions versus slowness.

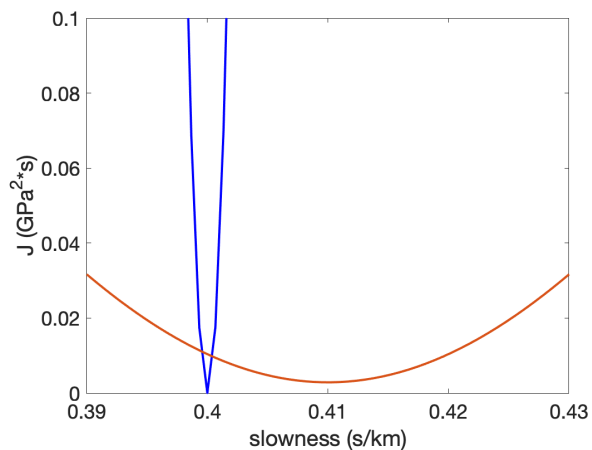


Figure 8. A zoomed-in plot of Figure 6 near the location of the global minimum.

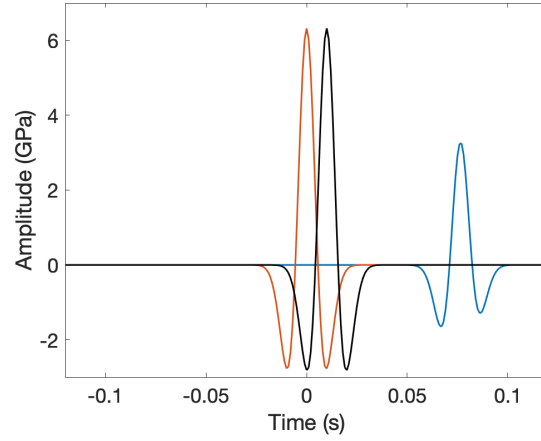


Figure 9. Estimated wavelets for Experiment 2a: Blue curve is the initial wavelet at $m = 1/3$, $\alpha = 1$. Red curve is the estimated wavelet at $m = 0.41$, $\alpha = 1$. The black curve is the target wavelet.

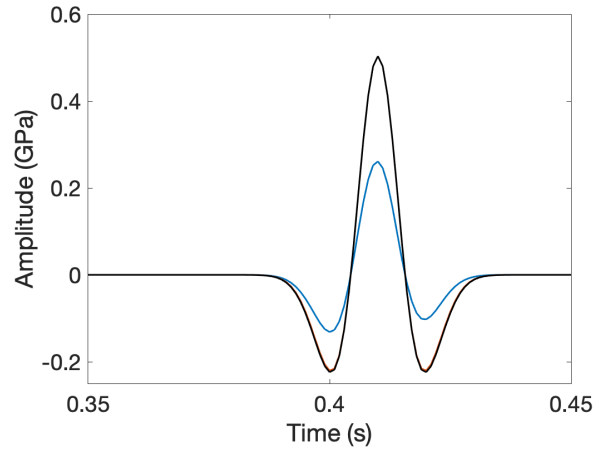


Figure 10. Estimated data for Experiment 2a: Blue curve is the initial data at $m = 1/3$, $\alpha = 1$. Red curve is the estimated data at $m = 0.41$, $\alpha = 1$. The black curve is the true data. Note that the red curve and black curve lay on top of each other and are, therefore, difficult to distinguish.

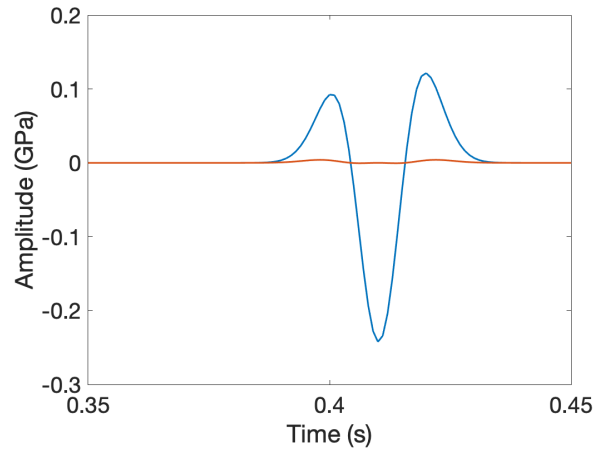


Figure 11. Residual $(F[m]w[m; d] - d)$ for Experiment 2a: Blue curve is the difference between the initial data and the true data. Red curve is the difference between the estimated data and the true data.

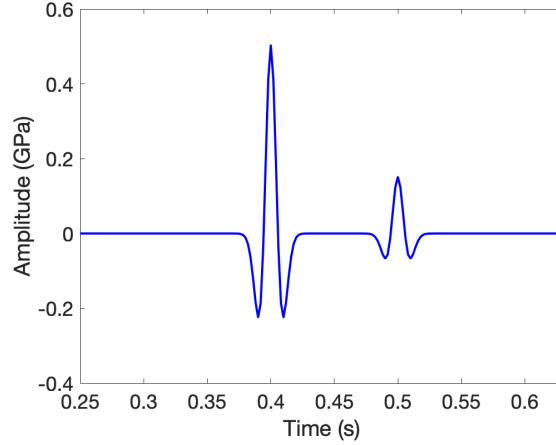


Figure 12. Data for experiment 3 produced by adding to the data of Figure 2 a shifted, scaled multiple of itself.

centered at $t = 0.5$ s. The noise-to-signal ratio is $\eta = 0.3$. With this choice of η and $\lambda = 0.025$ we obtain an upper bound on the error from inequality (13). Specifically,

$$|m - m_*| \leq \left(1 + \frac{2\eta(1 + \eta)}{1 - \eta(1 + \eta)} \right) \frac{\lambda}{r} \\ \approx 0.057.$$

The minimum m of the reduced ESI objective function is ≈ 0.401338 s/km as shown in Figure 13 and seen more clearly in Figure 14. The difference $|m - m_*| \approx 0.01338$ is substantially smaller than the upper error bound of 0.057 predicted by Result 2.

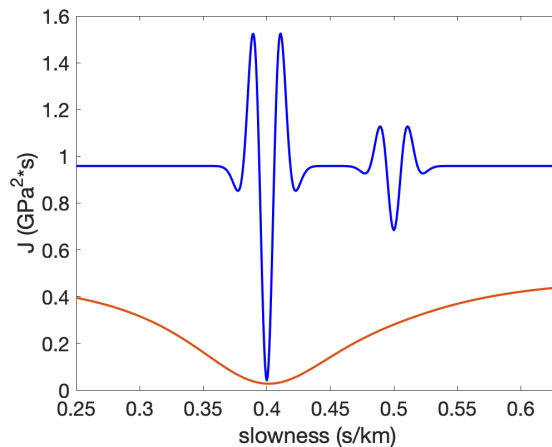


Figure 13. Experiment 3: The reduced FWI and ESI objective functions versus slowness.

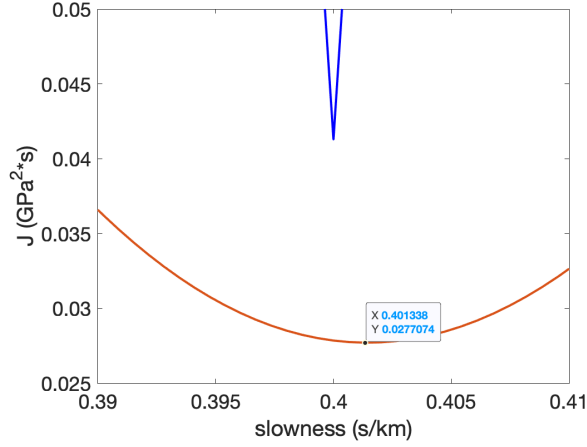


Figure 14. Experiment 3: A zoomed-in plot of Figure 13 near the global minimum.

Experiment 4: 100% Coherent Noise

We have already pointed out in the previous section that no result like inequality (13) in Result 2 could possibly hold for 100% (or more) noise, since that condition includes the case of noise that annihilates the signal, making the reduced ESI objective constant in m . Still it seems worth illustrating this point in a different way. The next example uses data similar to that of Experiment 3 but with larger noise that violates the hypotheses of Result 2. The data is given in Figure 15. The noise (centered at $t = 0.5$ s) is a shifted copy of the signal. Thus the signal to noise ratio is 1, which does not satisfy the assumption of Result 2 that $\eta < \frac{\sqrt{5}-1}{2}$. For this data, the reduced ESI objective function (with $\alpha = 1$) shown in Figure 16 exhibits multiple local (and global) minima. Both the target slowness ($m_* = 0.4$ s/km) and the slowness $m = 0.5$ s/km, that would be inferred if the noise were the entire signal, are near local minimizers.

Evidently this example could be modified, with similar results, by changing the time shift between the signal and the noise. Therefore the noise-to-signal ratio η does not bound the difference between the target slowness m_* and other stationary points of \tilde{J}_α . That is, no bound like that stated in Result 2 can possibly hold for noise levels this large.

Experiment 5: 100% Filtered Random Noise

We also mentioned in the last section that constraints on the type of noise may permit ESI to accurately estimate slowness and wavelet for noise-to-signal ratios higher than that permitted by Result 2. Figure 17 shows a data trace generated by adding to the signal in Figure 2 a band-limited

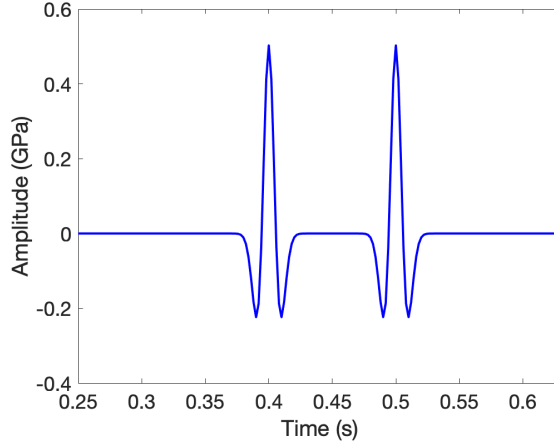


Figure 15. Experiment 4: data. Signal is same as shown in Figure 2 with the noise being a shifted copy of the signal.

uniformly distributed random noise trace with $\eta = 1$, which again violates the approximately 60% bound stated in Result 2. Inspection of the reduced ESI objective function (red curve in Figure 18) shows a unique local, and global, minimizer at almost precisely the target slowness used to generate the signal (Figure 2). The restricted FWI objective function (blue curve in Figure 18), on the other hand, has almost uniformly distributed local minima.

Despite their simplicity, these five experiments fully illustrate Result 2. More precisely, if the target wavelet w_* vanishes for $|t| > \lambda$ and the noise level η is below $\approx 60\%$, the reduced ESI objective has all of its stationary points within $O(\lambda) + O(\eta)$ of the *FWI* global minimum.

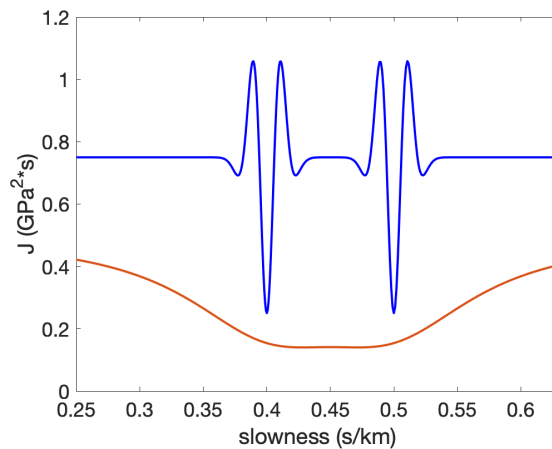


Figure 16. Experiment 4: The restricted FWI (blue curve) and reduced ESI (red curve) objective functions versus slowness.

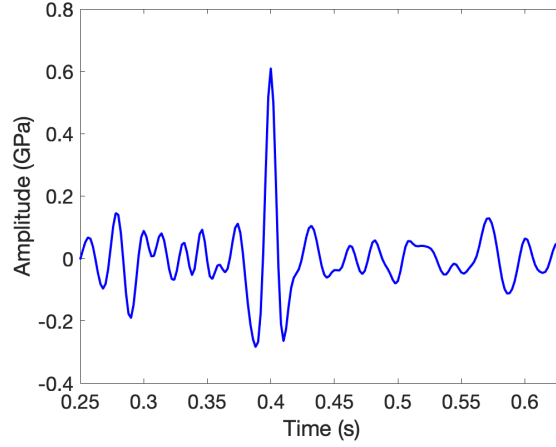


Figure 17. Experiment 5: data.

3.2 Discrepancy Algorithm and Solution of the Inverse Problem

None of the examples so far have taken the final step of truncation to the prescribed maximum lag λ necessary to produce a solution of the Inverse Problem as stated at the beginning of the last section. Also all of the examples discussed so far have employed a fixed, arbitrarily chosen penalty weight $\alpha = 1$. Since the penalty operator (multiplication by t) penalizes spread of energy away from $t = 0$, one would expect larger penalty weight to result in a smaller energy spread in the inverted wavelet, so less modification of the wavelet to conform to the maximum lag requirement of the Inverse Problem. The discrepancy algorithm increases α while maintaining data fit, so together with truncation of the wavelet at the prescribed lag (Result 3), should provide a route to solution of the inverse problem. The last two examples in this section illustrate Results 3 and 4.

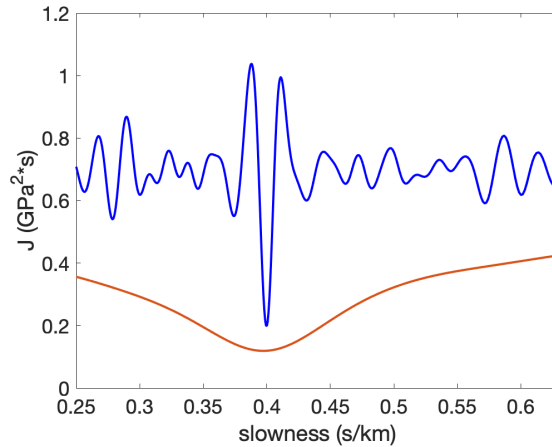


Figure 18. Experiment 5: Restricted FWI (blue curve) and reduced ESI (red curve) objective functions plotted versus slowness.

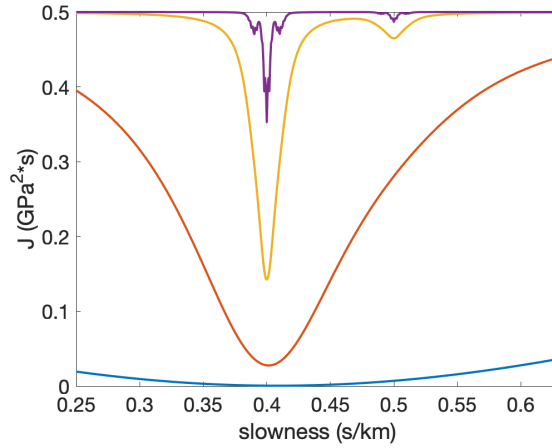


Figure 19. The reduced ESI objective function corresponding to the data shown in Figure 12 for various values of α . The blue curve corresponds to $\alpha = 0.1$. The red, yellow and purple curves correspond to $\alpha = 1.0, 10.0$ and 100.0 respectively.

We first discuss the selection of α . Figure 19 shows the reduced ESI objective function with various α values for the data given in Figure 12. The shape of the reduced ESI objective function changes drastically as α increases. For small α (blue curve in Figure 19), the objective function is very flat, but convex, with a unique stationary point. Achieving a small gradient (the usual stopping criterion for local optimization) for this choice of α will allow considerably more ambiguity in the estimated stationary point than does the same stopping criterion for a larger α (red, yellow or purple curves in Figure 19). This conclusion is partly captured in Result 4. Note that the yellow and purple curves exhibit local minimizers far from the target slowness, similar to reduced FWI. Evidently, α too small will inadequately constrain the slowness estimate, whereas α too large risks duplicating the behaviour of FWI. However, note that the local minimum values for large α , indeed all values of the objective, are quite large. Because the penalty term g decreases with α , whereas the data error e increases, the data error is the dominant contributor to these values for large α .

The discrepancy algorithm adjusts α dynamically to improve the rate of convergence and the accuracy of the model estimates obtained by ESI, while maintaining a prescribed level of data error. A proper constraint on data error prevents α from being increased beyond the level where multiple local minima appear.

The discrepancy algorithm requires that an acceptable range of data error ($[e_-, e_+]$) be prescribed. We use a relatively large range, based on a target signal-to-noise of 3. The actual signal-to-noise

iteration:	α	g	e
1	0.284184	0.371103	0.003140
2	0.568368	0.311447	0.022460
3	1.136737	0.204342	0.102216

Table 1. Experiment 6, discrepancy algorithm: α updates for initial $m = 0.343$. Initial $\alpha = 0$.

ratio in this example is ≈ 3.33 , corresponding to $e \approx 0.045$. We choose the error bounds for the discrepancy algorithm as $e_- \approx 0.027$, $e_+ \approx 0.11$.

Brent's method (Brent, 1971), used for the m update in the discrepancy algorithm, requires these inputs:

1. Initial search interval $[m_{\min}, m_{\max}]$: We use $m_{\min} = 0.33$, $m_{\max} = 0.65$ for every m update cycle;
2. A stopping tolerance for the gradient length: We use (absolute) tolerances of 0.01 for Experiment 6, 0.001 for Experiment 7.

Experiment 6: Coherent Noise

In this example, we use the data depicted in Figure 12. The progress of the algorithm is described in Tables 1-4. Table 1 shows the update of α using the rule 17 from the initial value $\alpha = 0$, attaining a value of e in the prescribed range after three iterations. Table 2 shows the first Brent's method update of m from its initial value of 0.343 s/km. It ends with an approximate stationary point of \tilde{J}_α having been found, and indeed a very good estimate of m_* . However the data error e has dropped below e_- , so another α update is necessary. As shown in Table 3, a single application of rule 17 is sufficient to bring e into compliance with the required bounds. Another 14 iterations of Brent's method (Table 4) compute another approximate stationary point of \tilde{J}_α . This time, the data error e also remains in the prescribed range, so the algorithm terminates.

Recall that the estimated wavelet $w_\alpha[m, d](t)$ (see Figure 20) is a solution of the normal equation given by Equation (11). The estimated data shown in Figure 21 is computed by $F[m]w_\alpha$ and its residual is shown in Figure 22.

Note that the estimated wavelet in Figure 20 does not satisfy the maximum lag constraint posed in the Inverse Problem. As explained in the last section, the second step of our algorithm

i :	g	e	m	\tilde{J}_α	$\frac{d}{dm}\tilde{J}_\alpha$
1	0.035018	0.403247	0.622695	0.448496	0.463686
2	0.089906	0.140974	0.478014	0.257147	2.614541
3	0.011959	0.017344	0.405674	0.032797	0.803269
4	0.028659	0.025577	0.381536	0.062608	-3.049986
5	0.009643	0.018478	0.400642	0.030938	-0.070100
6	0.010393	0.017888	0.403158	0.031317	0.370812
7	0.009914	0.018178	0.401900	0.030989	0.151012
8	0.009752	0.018327	0.401271	0.030929	0.040569
9	0.009691	0.018402	0.400956	0.030925	-0.014743
10	0.009720	0.018364	0.401114	0.030924	0.012919
11	0.009705	0.018383	0.401035	0.030924	-0.000911

Table 2. Experiment 6, discrepancy algorithm: updates of m after first update of $\alpha = 1.136737$. Initial $m = 0.343$.

for solution of the inverse problem is the truncation of the wavelet to a specified maximum lag. Result 3 gives estimates of both lag λ and data error ϵ , in terms of the maximum lag μ of the target wavelet w_* and the noise-to-signal ratio η , for which the conditions of the Inverse Problem should be satisfied by the truncated wavelet $w[m; d]$ at a stationary point m of \tilde{J}_α .

In this synthetic example, we can use the known values $\mu = 0.025$ and $\eta = 0.3$ in these estimates. However both estimates result from repeated use of the triangle inequality, and are very conservative. The estimated lag λ from inequality (14) is $\lambda = 0.082$, which turns out to be usable. Then the estimated wavelet is truncated to $[-\lambda, \lambda] = [-0.082, 0.082]$. This turns out to be a reasonable estimate for the truncation interval, as can be seen in plots of the truncated estimated wavelet (Figure 23), the data obtained by pairing this wavelet with the estimated slowness (Figure 24), and the resulting data residual (Figure 25).

On the other hand, the estimate (15) is quite pessimistic, estimating data error at nearly 100%. Instead, we simply compute the data error obtained with the estimated slowness and the truncated

iteration:	α	g	e	m
1	2.273473	0.009705	0.033737	0.401035

Table 3. Experiment 6, discrepancy algorithm: second update of α after first update of $m = 0.401035$. Initial $\alpha = 1.136737$.

i :	g	e	m	\tilde{J}_α	$\frac{d}{dm}\tilde{J}_\alpha$
1	0.002303	0.475832	0.637763	0.487735	0.114887
2	0.011948	0.336897	0.485548	0.398651	0.700990
3	0.007396	0.037167	0.409441	0.075396	5.288562
4	0.020844	0.111823	0.371387	0.219561	-7.541345
5	0.007280	0.040128	0.390414	0.077754	-5.521535
6	0.002986	0.033854	0.399927	0.049290	-0.128092
7	0.004197	0.034122	0.404684	0.055816	2.827748
8	0.003301	0.033728	0.402306	0.050789	1.382890
9	0.003068	0.033732	0.401116	0.049590	0.631507
10	0.003008	0.033779	0.400522	0.049327	0.252196
11	0.002992	0.033813	0.400225	0.049280	0.062106
12	0.002988	0.033833	0.400076	0.049278	-0.032988
13	0.002990	0.033823	0.400150	0.049278	0.014561
14	0.002989	0.033828	0.400113	0.049278	-0.009213

Table 4. Experiment 6, discrepancy algorithm: second update of m after second update of $\alpha = 2.273473$. Initial $m = 0.401035$. At the last iteration, the gradient norm termination criterion for Brent's method is satisfied, and the data error e is within the prescribed bounds, so the algorithm terminates.

wavelet just described. We obtain

$$\epsilon = \frac{\|F[m]\mathbf{1}_{[-\lambda, \lambda]}w - d\|}{\|d\|} \approx 0.29,$$

which is only slightly greater than the value obtained by substituting $m = m_*$, $w = w_*$.

Therefore we tentatively conclude that one should estimate a reasonable maximum lag λ

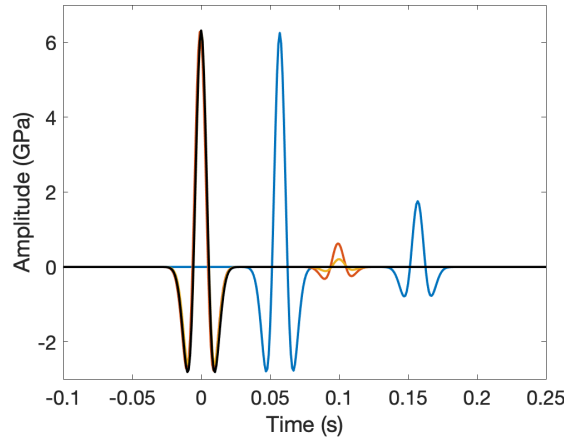


Figure 20. Experiment 6: Estimated wavelets $w_\alpha[m; d]$. Blue curve is the initial wavelet at $m = 0.343$, $\alpha = 0.284184$. Red curve is the estimated wavelet after the first update of m : $m = 0.401035$, $\alpha = 1.136737$. Yellow curve is the estimated wavelet after the second (final) update of m : $m = 0.400113$, $\alpha = 2.273473$. The black curve is the target wavelet.

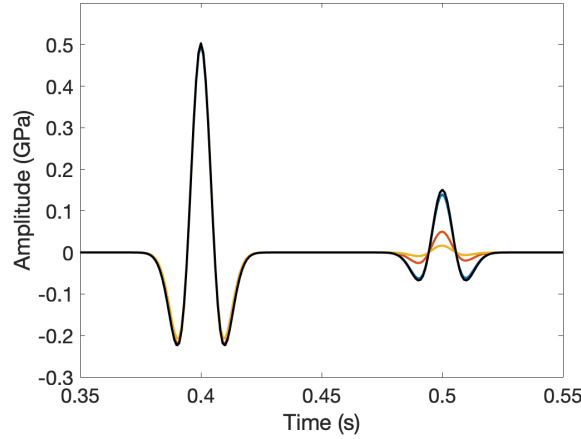


Figure 21. Experiment 6: estimated data $F[m]w_\alpha[m; d]$. Blue curve is the initial data at $m = 0.343$, $\alpha = 0.284184$. Red curve is the estimated data after the first update of m : $m = 0.401035$, $\alpha = 1.136737$. Yellow curve is the estimated data after the second (final) update of m : $m = 0.400113$, $\alpha = 2.273473$. The black curve is the true data.

via equation (14), truncate the wavelet, and then obtain the relative data error directly from the resulting predicted data, rather than relying on estimate 15.

Experiment 7: Filtered Random Noise

The data for this experiment is shown in Figure 26. It consists of the noise-free data shown in Figure 2, contaminated with uniformly distributed random noise, filtered by the noise-free wavelet and scaled to have noise-to-signal ratio $\eta = 0.3$, as in the previous example.

The course of the discrepancy algorithm is similar to that in the previous example, so we do not show the iterations in detail. Both α and m are updated twice, at which point a stationary

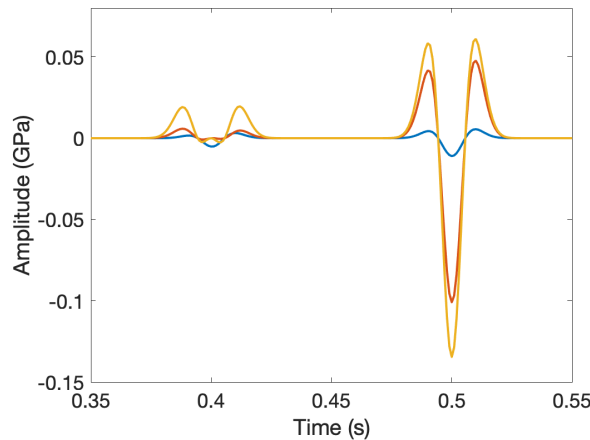


Figure 22. Experiment 6: Data Residual $(F[m]w_\alpha[m; d] - d)$. Blue curve is the difference between the initial data at $m = 0.343$, $\alpha = 0.284184$ and the true data. Red curve is the difference between the estimated data after the first update of m : $m = 0.401035$, $\alpha = 1.136737$ and the true data. Yellow curve is the difference between the estimated data after the second (final) update of m : $m = 0.400113$, $\alpha = 2.273473$ and the true data.

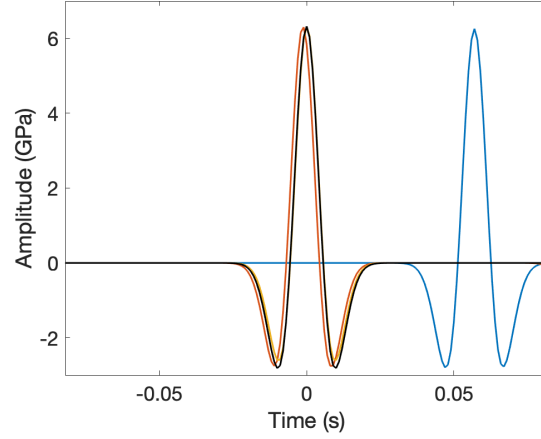


Figure 23. Experiment 6: Truncated estimated wavelets $\mathbf{1}_{[-\lambda, \lambda]} w_\alpha[m; d]$ for several iterates of the discrepancy algorithm. Blue curve is the initial wavelet at $m = 0.343$, $\alpha = 0.284184$. Red curve is the estimated wavelet after the first update of m : $m = 0.401035$, $\alpha = 1.136737$. Yellow curve is the estimated wavelet after the second (final) update of m : $m = 0.400113$, $\alpha = 2.273473$. The black curve is the target wavelet.

point of \tilde{J}_α has been found for which the bounds on e are satisfied. The estimated wavelet extends quite far from $t = 0$. The Figures 27, 28 and 29 show the wavelets, predicted data, and residuals respectively, computed in the course of two iterations.

Since μ and η are the same, the truncation lag estimated in Result 3 (equation (14)) is the same, namely $\lambda = 0.082$. Figures 30, 31 and 32 show the truncated wavelets and corresponding predicted data and residuals respectively, at the three iterates of the discrepancy algorithm. Computing the relative data error from the final residual shown in yellow in Figure 32, we conclude that the final

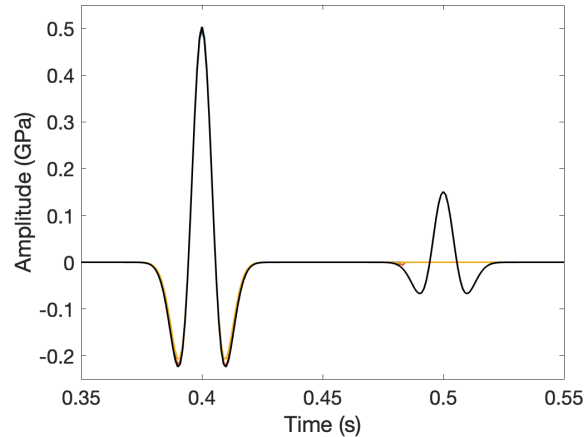


Figure 24. Experiment 6: predicted data from truncated wavelets, $F[m] \mathbf{1}_{[-\lambda, \lambda]} w_\alpha[m; d]$ for several iterates of the discrepancy algorithm. Blue curve is the initial data at $m = 0.343$, $\alpha = 0.284184$. Red curve is the estimated data after the first update of m : $m = 0.401035$, $\alpha = 1.136737$. Yellow curve is the estimated data after the second (final) update of m : $m = 0.400113$, $\alpha = 2.273473$. The black curve is the target data.

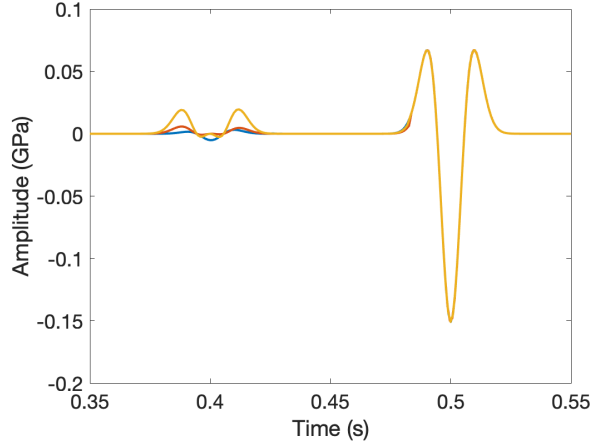


Figure 25. Experiment 6: data residual $(F[m]\mathbf{1}_{[-\lambda,\lambda]}w_\alpha - d)$ for several iterates of the discrepancy algorithm. Blue curve is the residual at the initial values $m = 0.343$, $\alpha = 0.284184$. Red curve is the residual after the first update of m : $m = 0.401035$, $\alpha = 1.136737$. Yellow curve is the residual after the second (final) update of m : $m = 0.400113$, $\alpha = 2.273473$.

slowness estimate $m = 0.400499$ and the final truncated wavelet (yellow curve in Figure 30) solve the Inverse Problem with $\lambda = 0.082$, $\epsilon = 0.27$.

4 DISCUSSION

The inverse problem discussed here is a drastic oversimplification of those encountered in various branches of seismology, as we have already pointed out. However it is a *subproblem* of many active source inverse problems: limit the data to a single source and a single receiver, mandate that the material model be spatially homogeneous, and a very similar problem emerges. Consequently, two

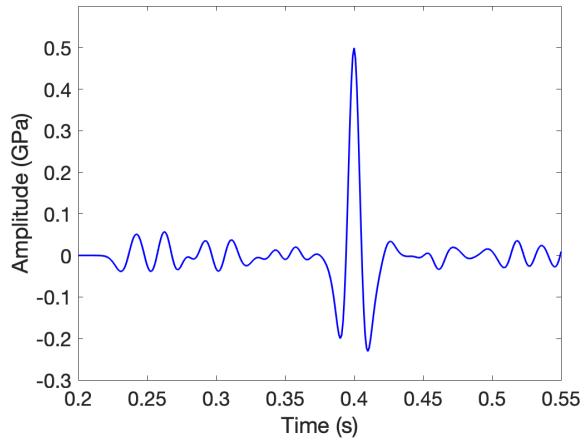


Figure 26. Experiment 7: data.

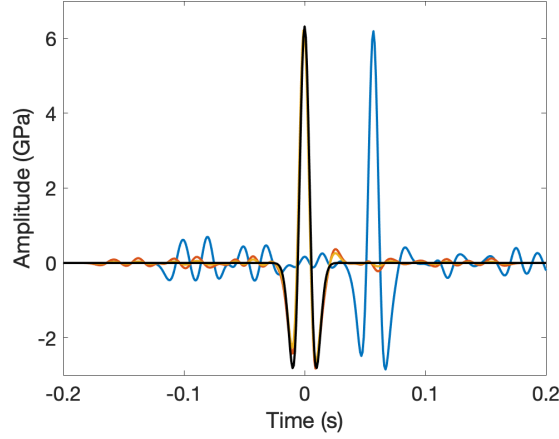


Figure 27. Experiment 7: Estimated wavelets $w_\alpha[m; d]$ for several iterations of the discrepancy algorithm. Blue curve is the initial wavelet at $m = 0.343$, $\alpha = 0.251370$. Red curve is the estimated wavelet after the first update of m : $m = 0.400444$, $\alpha = 1.005480$. Yellow curve is the estimated wavelet after the second (final) update of m : $m = 0.400499$, $\alpha = 2.010960$. The black curve is the target wavelet.

major implication for more complex and prototypical inverse problems emerge from the theory and examples presented here.

First, variable projection is not enough (to remedy the cycle skipping misbehaviour of standard FWI). Early contributions to the literature on VPM applied to seismic inversion concerned linearized or Born inversion, in which the linear degrees of freedom (analogous to the source wavelet here) are first order perturbations in material parameters (Symes & Gockenbach, 1995; van Leeuwen & Mulder, 2009). This approach appeared in other guises as Migration-Based Travel Time (MBTT) (Clément & Chavent, 1993) and Reflection FWI (RFWI) (Xu et al., 2012) algo-

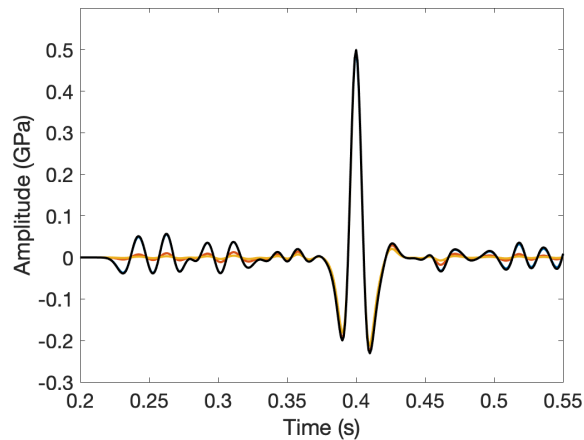


Figure 28. Experiment 7: Estimated data $F[m]w_\alpha[m; d]$. Blue curve is the initial data at $m = 0.343$, $\alpha = 0.251370$. Red curve is the estimated data after the first update of m : $m = 0.400444$, $\alpha = 1.005480$. Yellow curve is the estimated data after the second (final) update of m : $m = 0.400499$, $\alpha = 2.010960$. The black curve is the target data.

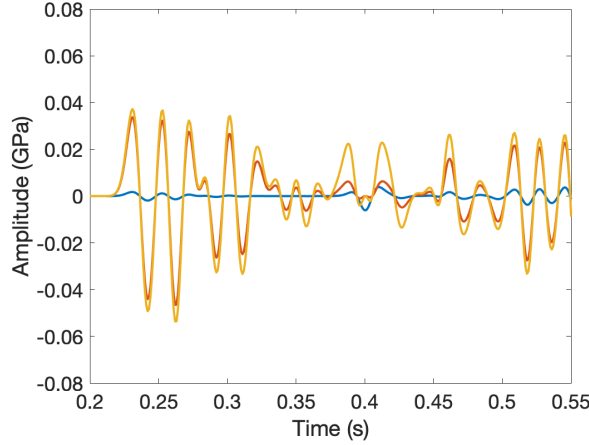


Figure 29. Experiment 7: Data residual $(F[m]w_\alpha[m; d] - d)$ for several iterations of the discrepancy algorithm. Blue curve is the residual at initial $m = 0.343$, $\alpha = 0.251370$. Red curve is the residual after the first update of m : $m = 0.400444$, $\alpha = 1.005480$. Yellow curve is the residual after the second (final) update of m : $m = 0.400499$, $\alpha = 2.010960$.

rithms. While these works suggest that VPM ameliorates the severe nonconvexity in the nonlinear degrees of freedom (velocity model) noted for basic FWI for reflection data, this mitigation is limited in extent, and cycle-skipping can still occur (Huang, 2016). VPM reduction of FWI via elimination of source parameters has been suggested for example by Rickett (2012); Aravkin & van Leeuwen (2012); Li et al. (2013); Tu et al. (2016) and van Leeuwen & Aravkin (2020), in various contexts. Result 1 and Figures 6 and 7 show that for inversion based on transmitted data,

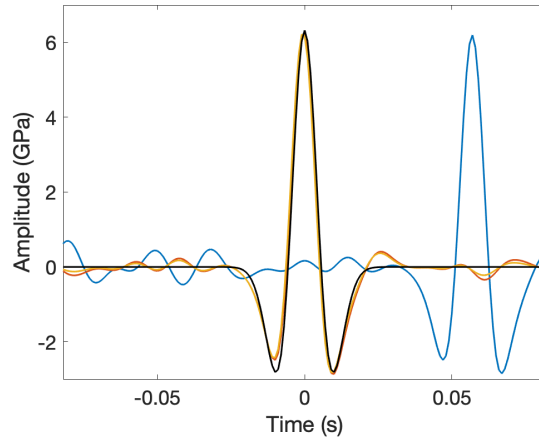


Figure 30. Experiment 7: Truncated estimated wavelets $\mathbf{1}_{[-\lambda, \lambda]}w_\alpha[m; d]$, $\lambda = 0.082$ for several iterations of the discrepancy algorithm. Blue curve is truncated wavelet at initial $m = 0.343$, $\alpha = 0.251370$. Red curve is the truncated wavelet after the first update of m : $m = 0.400444$, $\alpha = 1.005480$. Yellow curve is the truncated wavelet after the second (final) update of m : $m = 0.400499$, $\alpha = 2.010960$. The black curve is the target wavelet.

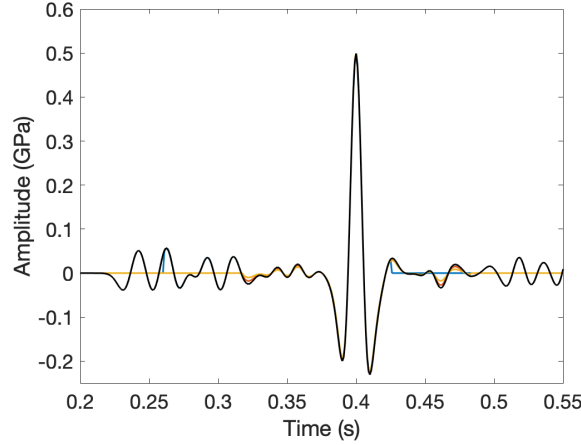


Figure 31. Experiment 7: Estimated data from truncated wavelets, $F[m]\mathbf{1}_{[-\lambda,\lambda]}w_\alpha[m;d]$ for several iterations of discrepancy algorithm. Blue curve is the initial data at $m = 0.343$, $\alpha = 0.251370$. Red curve is the estimated data after the first update of m : $m = 0.400444$, $\alpha = 1.005480$. Yellow curve is the estimated data after the second (final) update of m : $m = 0.400499$, $\alpha = 2.010960$. The black curve is the target data.

VPM reduction via elimination of source parameters may fail to produce an optimization problem more tractable than basic FWI.

Second, the explicit expression 19 for the gradient of \tilde{J}_α is actually a special case of a generic calculation valid for similar reduced objective functions, based on a large class of forward maps F , as explained by Symes et al. (2020) and Symes (2022), Appendix. This class includes models of transmission through transparent (non-scattering) material models, of which our $F[m]$ is the simplest possible case, and some models of single scattering (ten Kroode, 2014; Symes, 2014). These calculations, and the features of the reduced objective that they reveal, are responsible for

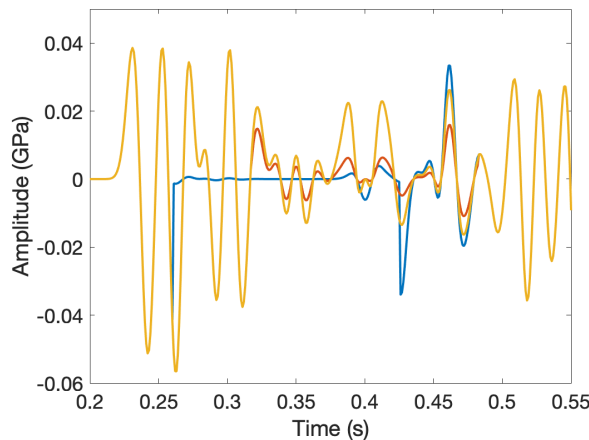


Figure 32. Experiment 7: Data residual using truncated wavelets $(F[m]\mathbf{1}_{[-\lambda,\lambda]}w_\alpha[m;d] - d)$ for several iterations of the discrepancy algorithm. Blue curve is initial residual at $m = 0.343$, $\alpha = 0.251370$. Red curve is residual after the first update of m : $m = 0.400444$, $\alpha = 1.005480$. Yellow curve is residual after the second (final) update of m : $m = 0.400499$, $\alpha = 2.010960$.

the feasibility of the VPM approach. We refer the reader to the cited references for the technical details, and to Huang et al. (2019) and references cited there for numerical illustration in more complex settings.

In the discussion of Experiment 5, we mentioned that the constraint on noise level posed in Result 2 is not always necessary for good convergence to an accurate slowness estimate. Result 2 presumes a worst-case constructive buildup of noise impact on \tilde{J}_α : while sharp, the result may be far too pessimistic for generic noisy data. In particular, Experiment 5 suggests that uniform filtered random noise in large quantities (greater than 100%) still permits fairly precise determination of slowness. A close reading of the analysis underlying Result 2 (Symes, 2022) gives some hint about why this might be so, but much remains to be understood about noise statistics and their interaction with the solution of the inverse problem.

Result 4 motivates the use of the discrepancy algorithm but does not really explain its performance. Symes (2021), Appendix A, clarifies the properties of the α update part of the algorithm, but the interaction with the m update remains obscure, and no convergence result is proven for the algorithm as a whole in that work.

The selection of the error range $[e_-, e_+]$ for the discrepancy algorithm has so far been entirely ad-hoc, both in earlier work (Fu & Symes, 2017) and in the experiments reported here. In almost all practical applications of inverse theory, the actual data signal-to-noise ratio is a priori unknown. What is the behaviour of the discrepancy algorithm when the upper error bound e_+ is chosen too low, relative to the actual noise level in the data? Or the lower error bound e_- too high? Is it possible to recover from erroneous choice of these parameters, or to learn anything about the actual noise level from the behaviour of the discrepancy algorithm? These questions remain to be investigated.

5 CONCLUSION

We introduced a single-trace acoustic transmission inverse problem, that (despite its simplicity) exhibits one of the fundamental pathologies of real-world full waveform inversion (FWI), namely, cycle-skipping: the standard least-squares objective function of FWI tends to have many stationary

points, most of them far from any physically relevant model, so that local optimization produces uninformative model estimates.

We have reviewed the theory of extended source inversion (ESI) applied to this problem. This theory suggests that the ESI approach avoids cycle-skipping, and enables the computation of accurate solutions using standard local optimization methods. Our numerical examples illuminate the extent to which the theory accurately predicts the performance of ESI in concrete instances. Allowing for the inevitable worst-case flavor of such theory, the conformance of theory and example is reasonably good. In particular, stationary points of the ESI objective function lie near the global minimizer of the usual (FWI) least-squares objective function, with error bounded by a multiple of the wavelet width and the RMS noise level in the data. Extended source inversion involves a penalty formulation so is incomplete without some method for selection of the penalty weight parameter. We presented an algorithm based on the discrepancy principle for adjustment of this parameter, and used it in examples to produce a solution of the inverse problem.

6 ACKNOWLEDGEMENTS

This research is partially supported by the sponsors of the UT Dallas “3D+4D Seismic FWI” research consortium.

7 DATA AVAILABILITY STATEMENT

The data that support the findings of this study are available upon reasonable request from the authors.

References

- Aghmiry, H., Gholami, A., & Operto, S., 2020. Accurate and efficient data-assimilated wavefield reconstruction in the time domain, *Geophysics*, **85**, A7–A12.
- Aravkin, A. & van Leeuwen, T., 2012. Estimating nuisance parameters in inverse problems, *Inverse Problems*, **28**, 115016.
- Bertero, M. & Boccacci, P., 1998. *Introduction to Inverse Problems in Imaging*, CRC Press, New York.
- Biondi, B. & Almomin, A., 2012. Tomographic full waveform inversion (TFWI) by combining full waveform inversion with wave-equation migration velocity analysis, in *Expanded Abstracts*, p. SI9.5, Society of Exploration Geophysicists.
- Brent, R., 1971. An algorithm with guaranteed convergence for finding a zero of a function, *The Computer Journal*, **14**, 422–425.
- Chauris, H. & Cocher, E., 2017. From migration to inversion velocity analysis, *Geophysics*, **82**, S207–S223.
- Clément, F. & Chavent, G., 1993. Waveform inversion through MBTT formulation, in *Mathematical and Numerical Aspects of Wave Propagation*, eds Kleinman, E., Angell, T., Colton, D., Santosa, F., & Stakgold, I., Society for Industrial and Applied Mathematics, Philadelphia.
- Courant, R. & Hilbert, D., 1962. *Methods of Mathematical Physics, Volume II*, Wiley-Interscience, New York.
- Engl, H., Hanke, M., & Neubauer, A., 1996. *Regularization of inverse problems*, Kluwer Academic Publishers, New York.
- Fichtner, A., 2010. *Full Seismic Waveform Modelling and Inversion*, Springer Verlag, Berlin.
- Friedlander, F., 1958. *Sound Pulses*, Cambridge University Press.
- Fu, L. & Symes, W. W., 2017. A discrepancy-based penalty method for extended waveform inversion, *Geophysics*, **82**, R287–R298.
- Gauthier, O., Tarantola, A., & Virieux, J., 1986. Two-dimensional nonlinear inversion of seismic waveforms, *Geophysics*, **51**, 1387–1403.
- Golub, G. & Pereyra, V., 1973. The differentiation of pseudoinverses and nonlinear least squares

- problems whose variables separate, *SIAM Journal on Numerical Analysis*, **10**, 413–432.
- Golub, G. & Pereyra, V., 2003. Separable nonlinear least squares: the variable projection method and its applications, *Inverse Problems*, **19**, R1–R26.
- Hanke, M., 2017. *A Taste of Inverse Problems*, Society for Industrial and Applied Mathematics, Philadelphia.
- Huang, G., Nammour, R., Symes, W., & Dollizal, M., 2019. Waveform inversion by source extension, in *Expanded Abstracts*, pp. 4761–4765, Society of Exploration Geophysicists.
- Huang, Y., 2016. *Born Waveform Inversion in Shot Coordinate Domain*, Ph.D. thesis, Rice University.
- Lameloise, C.-A., Chauris, H., & Noble, M., 2015. Improving the gradient of the image-domain objective function using quantitative migration for a more robust migration velocity analysis, *Geophysical Prospecting*, **63**, 391–404.
- Li, M., Rickett, J., & Abubakar, A., 2013. Application of the variable projection scheme to frequency-domain full-waveform inversion, *Geophysics*, **78**(6), R249–R257.
- Liu, Y., Symes, W., & Li, Z., 2014. Inversion velocity analysis via differential semblance optimization, in *Extended Abstracts*, European Association of Geoscientists and Engineers.
- Luo, S. & Sava, P., 2011. A deconvolution-based objective function for wave-equation inversion, in *Expanded Abstracts*, pp. 2788–2792, Society of Exploration Geophysicists.
- Mahankali, S. & Yang, Y., 2021. The convexity of optimal transport-based waveform inversion for certain structured velocity models, <https://www.siam.org/Portals/0/Documents/S136187PDF.pdf?ver=2021-03-18-120457-860>.
- Métivier, L. & Brossier, R., 2020. A receiver-extension approach to robust full waveform inversion, in *Expanded Abstracts*, pp. 641–645, Society of Exploration Geophysicists.
- Métivier, L., Allain, A., Brossier, B., Mérigot, Q., Oudet, E., & Virieux, J., 2018. Optimal transport for mitigating cycle skipping in full-waveform inversion: A graph-space transform approach, *Geophysics*, **83**, R515–R540.
- Parker, R., 1994. *Geophysical Inverse Theory*, Princeton University Press, Princeton.
- Plessix, R.-E., Mulder, W., & ten Kroode, F., 2000. Automatic cross-well tomography by sem-

- blance and differential semblance optimization: theory and gradient computation, *Geophysical Prospecting*, **48**(5), 913–935.
- Plessix, R.-E., Baeten, G., de Maag, J. W., Klaassen, M., Zhang, R., & Tao, Z., 2010. Application of acoustic full waveform inversion to a low-frequency large-offset land data set, in *Expanded Abstracts*, pp. 930–934, Society of Exploration Geophysicists.
- Rickett, J., 2012. The variable projection method for waveform inversion with an unknown source function, in *Expanded Abstracts*, pp. 1–5, Society of Exploration Geophysicists.
- Schuster, G., 2017. *Seismic Inversion*, Society of Exploration Geophysicists, Tulsa.
- Sheriff, R. E. & Geldart, L. P., 1995. *Exploration Seismology*, Cambridge University Press.
- Symes, W., 2008. Migration velocity analysis and waveform inversion, *Geophysical Prospecting*, **56**, 765–790.
- Symes, W., 2009. The seismic reflection inverse problem, *Inverse Problems*, **25**, 123008:1–24.
- Symes, W., 2014. Seismic inverse problems: recent developments in theory and practice, in *Proceedings*, pp. 2–5, Institute of Physics.
- Symes, W., 2020. Wavefield reconstruction inversion: an example, *Inverse Problems*, **36**, 105010, <https://dx.doi.org/10.1088/1361-6420/abaf66>.
- Symes, W., 2021. Solution of an acoustic transmission inverse problem by extended inversion: theory, arXiv:2110.15494v1.
- Symes, W., 2022. Error bounds for extended source inversion applied to an acoustic transmission inverse problem, arXiv:2110.15494v2.
- Symes, W. & Carazzone, J. J., 1991. Velocity inversion by differential semblance optimization, *Geophysics*, **56**(5), 654–663.
- Symes, W. & Gockenbach, M., 1995. Waveform inversion for velocity: Where have all the minima gone?, in *Expanded Abstracts*, pp. 1235–1239.
- Symes, W. & Hou, J., 2018. Inversion velocity analysis in the subsurface offset domain, *Geophysics*, **83**, R189–R200.
- Symes, W., Chen, H., & Minkoff, S., 2020. Full waveform inversion by source extension: why it works, in *Expanded Abstracts*, pp. 765–769, Society of Exploration Geophysicists.

- Tarantola, A., 2005. *Inverse Problem Theory and Model Parameter Estimation*, Society for Industrial and Applied Mathematics, Philadelphia.
- ten Kroode, F., 2014. A Lie group associated to seismic velocity estimation, in *Proceedings*, pp. 142–146, Institute of Physics.
- Tu, N., Aravkin, A., van Leeuwen, T., Lin, T., & Herrmann, F. J., 2016. Source estimation with surface-related multiples—fast ambiguity-resolved seismic imaging, *Geophysical Journal International*, **205**(3), 1492–1511.
- van Leeuwen, T. & Aravkin, A., 2020. Non-smooth variable projection, arXiv:1601.05011.
- van Leeuwen, T. & Herrmann, F., 2013. Mitigating local minima in full-waveform inversion by expanding the search space, *Geophysical Journal International*, **195**(1), 661–667.
- van Leeuwen, T. & Herrmann, F., 2016. A penalty method for pde-constrained optimization in inverse problems, *Inverse Problems*, **32**, 1–26.
- van Leeuwen, T. & Mulder, W., 2009. A variable projection method for waveform inversion, in *Extended Abstracts*, p. U024, European Association of Geoscientists and Engineers.
- Virieux, J. & Operto, S., 2009. An overview of full waveform inversion in exploration geophysics, *Geophysics*, **74**, WCC127–WCC152.
- Vogel, C., 2002. *Computational Methods for Inverse Problems*, Society for Industrial and Applied Mathematics, Philadelphia.
- Warner, M. & Guasch, L., 2014. Adaptive waveform inversion: Theory, in *Expanded Abstracts*, pp. 1089–1093, Society of Exploration Geophysicists.
- Warner, M. & Guasch, L., 2016. Adaptive waveform inversion: theory, *Geophysics*, **81**(6), R429–R445.
- Xu, S., Wang, D., Chen, F., Zhang, Y., & Lambare, G., 2012. Full waveform inversion for reflected seismic data, in *Expanded Abstracts*, European Association for Geoscientists and Engineers, Copenhagen.
- Yang, Y., Engquist, B., Sun, J., & Hamfeldt, B., 2018. Application of optimal transport and the quadratic Wasserstein metric to full-waveform inversion, *Geophysics*, **83**, R43–R62.
- Yilmaz, O., 2001. Seismic data processing, in *Investigations in Geophysics No. 10*, Society of

Exploration Geophysicists, Tulsa.

Ziolkowski, A., Parkes, G., Hatton, L., & Haugland, T., 1982. The signature of an air gun array: Computation from near-field measurements including interactions, *Geophysics*, **47**, 1413–1421.